Wireless Magnetoelastic Monitoring of Biliary Stents

Scott R. Green and Yogesh B. Gianchandani

Abstract—This paper presents a system for wirelessly monitoring the accumulation of sludge in a biliary stent. Two generations of the system are detailed. The first-generation system utilizes a 2×37.5-mm ribbon sensor with a mass of 18 mg, along with 0.8-mm-thick $\times$ 1.6-mm-diameter neodymium magnets to bias the sensor. Both components are integrated with a 4-mm-diameter stainless steel stent. The second-generation system comprises a sensor and a magnetic layer [consisting of strontium ferrite particles suspended in polydimethylsiloxane (PDMS)] that conform to the meshed topology and tubular curvature of a 5-mm-diameter Elgiloy stent. The second-generation sensors have an active area of 7.5×29 mm and a mass of 9.1 mg. The sensors in both generations are fabricated from 28-μm-thick foils of magnetoelastic 2826MB Metglas, an amorphous Ni–Fe alloy. Analytical and finite-element models that predict sensor response in the dynamic biological environment are presented. The response of each system to viscosity changes that precede and accompany biliary sludge accumulation is tested, with resonant frequency changes of 2.8% and 6.5% over a 10-cP range for each respective generation. Sludge accumulation is simulated with successive coatings of either paraffin or an acrylate terpolymer. Resonant frequency response to this mass loading effect is similar for both generations of the system, showing a 40% decrease after applying a mass load of $2.5\times$ the mass of the sensor.   **[2008-0154]**

Index Terms—Elgiloy, magnetoelasticity, Metglas, microsensors, photochemical machining, resonant sensors.

I. INTRODUCTION

STENTS are tubular structures used to impart and maintain patency in a variety of vessels and ducts that have become constricted as a result of stenotic pathology. Although the act of implanting a stent relieves symptoms caused by the constriction, in-stent restenosis—a reappearance of the narrowing, typically due to the reaction of the body to the presence of the stent—is a risk associated with all stenting procedures.

An example of a stent application area—and the focus of this paper—is the bile duct, which transports bile between the liver, gall bladder, pancreas, and small intestine. Bile is used in the intestinal tract for the emulsification and absorption of fats. The constriction relieved by stent implantation is often due to pancreatitis, cholangitis, tumors, or gallstones. Restenosis

Fig. 1. Pathology of biliary restenosis subsequent to stent placement. (A) Self-expanding stent initially relieves duct constriction. (B) Protein layer forms on the surfaces of the stent. (C) Protein layer allows bacteria to adhere to the stent surfaces. (D) Bacteria generate a mucopolysaccharide matrix, commonly termed "biliary sludge." (E) Sludge accumulates, leading to a narrowed-duct condition.

can occur in an average of four to five months via formation of a bacterial matrix on and around the stent. This bacterial matrix is known as biliary "sludge" [1]. The pathology of sludge formation (Fig. 1) begins with the formation of a protein layer—including fibronectin and collagen—on the stent surfaces. Bacteria present in the bile, including *Escherichia coli* and *Enterococcus*, tend to adhere to the protein. As these bacteria congregate, they produce an extracellular biofilm and matrix. Additionally, the bacteria release enzymes that precipitate crystals of cholesterol and calcium bilirubinate (among others) out of solution; these crystals become trapped in the matrix. Collectively, the matrix, crystals, biofilm, and bacteria are termed "biliary sludge." This sludge accumulates and eventually leads to occlusion of the duct which, of course, is the same situation that required the stent implantation. Current medical techniques for dealing with sludge accumulation include either replacing the stent while clearing the sludge or simply implanting a second stent inside of the first.

Various methods for the prevention of biliary stent clogging have been investigated. These methods include using stent materials with different levels of hydrophilicity or even materials impregnated with antimicrobial agents. Alternatively, patients have been administered prophylactic antibiotics in an attempt to kill bacteria before their attachment to the stent. Anticlogging mechanical features such as side holes (or lack of side holes) or a unidirectional valve mechanism (to prevent influx of bacteria-laden fluids) have also been tested. To date, each of these methods has achieved mixed results that are not yet at the level of clinical relevance. Clearly, restenosis is a recalcitrant issue. Since prevention of restenosis cannot be assured, the patient must be monitored to ensure continued patency of the bile duct.

The time frame for clinically significant restenosis to occur is highly variable from case to case. Current techniques for diagnosing a blockage use a blood test to monitor enzymes such
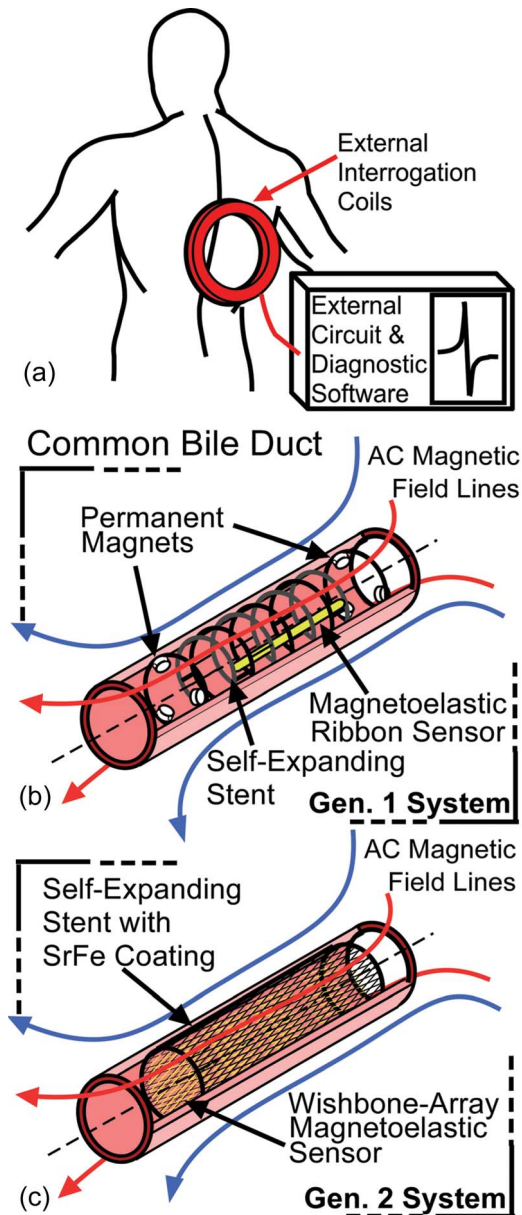
Fig. 2. Conceptual diagram of two generations of *in vivo* magnetoelastic sensing of sludge accumulation for biliary stents. (a) External circuitry drives the external interrogation coils to wirelessly measure the response of the implanted sensor. (b) In the generation-1 system, the discrete neodymium magnets bias the ribbon sensor. (c) In the generation-2 system, the distributed SrFe permanent-magnet layer biases the wishbone-array sensor for optimal signal and does not hinder the stent mechanical operation.

as bilirubin and alkaline phosphatase, among others. Imaging of the duct—using either computed tomography or endoscopic cholangiography—then confirms the presence of a blockage. These techniques for diagnosing a blockage are indirect and rely on detecting enzyme levels that may not increase until after the blockage is significant. The combined effect of the unknown time course for restenosis and the indirect testing methods can result in either unnecessary prescheduled interventions or untimely interventions after patients exhibit outward symptoms of the blockage, such as jaundice or pruritus. As such, a direct method of diagnosis would enable timely intervention and eliminate unnecessary procedures. The method outlined in Fig. 2,

highlighting two generations of an integrated system, provides just such a direct measurement of sludge accumulation in a biliary stent. A network analyzer controls an amplifier, driving the transmit coils in an ac frequency sweep that produces a corresponding magnetic field sweep. The magnetic field causes a magnetoelastic sensor integrated with the stent to resonate at a frequency that changes as local viscosity increases and as sludge accumulates. The mechanical resonance generates an oscillating magnetic flux that can be measured with an external pickup coil. The frequency content of the induced voltage can then be correlated to the local sensor environment.

We have previously reported a "smart stent" for cardiovascular applications [2] which utilizes variable capacitance pressure sensors connected to an inductive "stentenna" to form a wireless resonant LC tank. The pressure drop measured across the stent can then be correlated with the flow through the stent. For coronary stents, flow rates of 100–200 mL/min are expected, with average pressures of $\sim$100 mmHg. In contrast, flow rates in biliary stents are 3–4 mL/min after meals and $\sim$1 mL/min on average, while pressure differences and average pressures are on the order of 10–30 mmHg [3], [4]. Measurement of flow and pressure is thus a much more difficult task in biliary stents than in cardiovascular stents, and pressure changes are less correlated with disease states. Investigation into alternative transduction methods for biliary applications is thus warranted.

Past work in magnetoelastic sensors has demonstrated the feasibility of sensing mass loading, media viscosity, and other properties in environmental/industrial applications [5]–[8]. An early device utilizing the magnetoelastic transduction pathway consisted of NiFe films sandwiched around a chemically sensitive polymer layer, the swelling of which affected the amplitude and shape of the induced voltage pulse train [5]. The device was not used as a resonant sensor.

Resonant sensors have the relative advantages of immunity to noise and changes in the amplitude or orientation of the interrogation field. Due to these advantages, later work in magnetoelastic sensors used the measured resonant frequency to correlate with properties of either the surrounding media or with properties in the sensor material or an analyte layer on the sensor. Examples of the former properties include density, viscosity [6], [7], and pressure [8] in a surrounding fluid layer, while examples of the latter properties include thermal coefficients (to measure temperature) of the sensor material or analyte layer stiffness or density (to measure the presence of a target chemical species). Recent work with magnetoelastic sensors has explored acute measurement of gastroesophageal pH with instrumented ingested capsules [9]. In each of these cases, the stiffness, mass, or damping of the system is altered in some way, and these general parameters directly govern the resonant frequency. Reviews on magnetoelastic sensors were published in 2002 [10] and more recently in 2007 [11].

An important feature of magnetoelastic sensors in the context of implantable devices is the ability to be wirelessly interrogated. This paper[1] presents an integrated system for wirelessly monitoring the accumulation of sludge in a biliary stent. Two

---

[1]Portions of this paper have appeared in conference abstract form in [12]–[14].

generations of the system are detailed, the first comprising a magnetoelastic ribbon sensor and biasing discrete permanent magnets, and the second comprising a sensor and biasing permanent-magnet layer that conform to the meshed topology and tubular curvature of a biliary stent. Modeling tools for resonant magnetoelastic sensors are first described, followed by specific design and fabrication information. Finally, experimental methods and results are delineated.

II. MODELING

A. General Considerations

Magnetoelastic behavior is most prominent in materials with elongated magnetic domains [15]. Under an applied magnetic field, these domains tend to rotate and align with the field. As the long axes of the domains rotate and align, the material experiences strain. The magnetization of the material also responds to the applied field. For magnetoelastic materials used as resonant sensors, the oscillating magnetic flux developed as a result of oscillating strain in the sensor can then induce a voltage on a suitably located pickup coil.

Although magnetoelastic materials are generally nonlinear, it is prudent to use linearized constitutive equations describing the coupling between flux density, field strength, stress, and strain in a magnetostrictive material

$$\vec{\sigma} = [C]\vec{\varepsilon} - \frac{[C][d]^T}{\mu_o \mu_r}\vec{B} \qquad (1)$$

$$\vec{H} = -\frac{[d][C]}{\mu_o \mu_r}\vec{\varepsilon} + \frac{1}{\mu_0 \mu_r}\vec{B}. \qquad (2)$$

Equations (1) and (2) are versions of the so-called "piezomagnetic" equations [16], where σ is the vectorized stress tensor, C is the stiffness matrix, ε is the vectorized strain tensor, d is the magnetostrictivity matrix, B is the magnetic flux density vector, H is the field strength vector, μ_0 is the permeability of free space, and μ_r is the relative permeability (assumed isotropic here).

Typical "transfer characteristics" relating the strain to the applied field for zero prestress in three grades of amorphous metals—primarily nickel–iron alloys—sold under the trade name Metglas [17] are shown in Fig. 3 (using data provided in [18]–[20]). Note that hysteresis effects that are present in these curves are omitted for clarity. The derivative of the curve at the chosen bias field gives the magnetostrictivity. The amorphous nature of the materials results in isotropic magnetostrictivity. Other important properties of these materials are listed in Table I. The high permeability of these materials enhances the antenna-like nature of the sensor by attracting flux lines and directing them along the length of the sensor, which is desirable in that the orientation of the interrogating signal is not required to be exactly along the length of the sensor for good response. However, the high permeability can also be a disadvantage in that it limits how effectively the interrogative field can penetrate the sensor and how effectively the sensor can emit flux. In fact, both the analytical and finite-element models described in
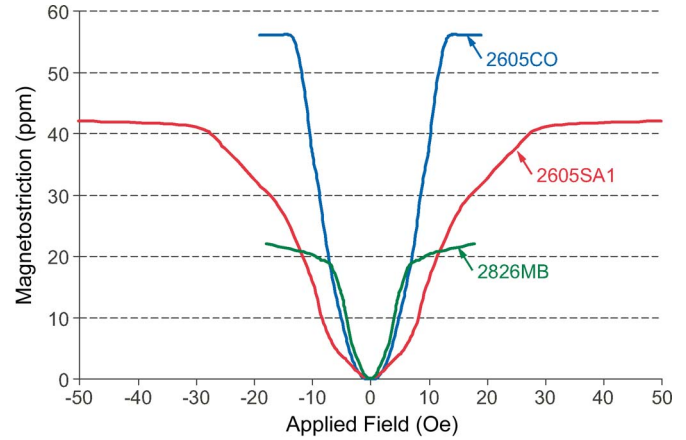
Fig. 3. Magnetostriction versus applied field for various amorphous metals (reproduced from [18]–[20]). The illustrated curves are from materials after annealing in a transverse magnetic field. The derivative of these curves evaluated at a bias point leads to the small-signal magnetostrictivity ("d") for the material at that bias point. These plots can be helpful for choosing between various alloys; however, they are generally established with low-frequency (quasi-static) stimulating fields and thus provide incomplete information about material behavior near resonance [19].

part B of this section predict that the signal output of the sensor is inversely proportional to the permeability.

The choice of a bias field determines not only the small-signal magnetostrictivity but also the apparent Young's modulus of the material. The dependence of the Young's modulus on the applied field is termed the "ΔE effect." The ΔE effect is a direct result of the magnetomechanical coupling properties of the material [21] and can be quite substantial in amorphous metals. For example, the listed (i.e., unbiased) Young's modulus for the 2826MB alloy is 100–110 GPa. For bias fields near 1 Oe in a transversely annealed sample, the modulus can vary by 21–31 GPa/Oe [22]. Thus, small changes in the bias field can result in large changes in the Young's modulus. For a resonant sensor, this effect is particularly important, as the resonant frequency is roughly proportional to the square root of the Young's modulus. As such, providing a consistent biasing field to the sensor is crucial to minimizing a significant source of repeatability error. In fact, minimizing the ΔE effect is the main driver for integrating the biasing magnetic components with the stent in our system, as will be further discussed in Section III.

Past studies of the magnetoelastic properties of amorphous metals often include annealing the material (e.g., [18]–[20], [22], and [23]). In general, this procedure improves the magnetomechanical coupling coefficient, which is a measure of the efficiency of the material in converting between magnetic energy and elastic energy. In this paper, the response of the sensors to thermal treatment is explored. Inclusion of a large transverse dc magnetic field during the treatment may improve the signal amplitude further but is outside the scope of this paper.

It should be noted that amorphous metals are not the only materials that exhibit large magnetostriction. In fact, so-called "giant magnetostrictive materials" (GMMs)—rare-earth–iron alloys like Terfenol-D (terbium, iron, and dysprosium) and Galfenol (gallium and iron)—have been recently explored in transducer applications, e.g., in [15] and [24]. However, when compared with amorphous metals in our application,

Alloy	Composition	Density (kg/m³)	Thickness (μm)	DC Relative Permeability	Saturation Magnetostriction (ppm)	Saturation Induction (T)	Saturation Bias Field (Oe)
2826MB	FeNiMoB	7900	29.2	>50000	12	0.88	8
2605CO	FeCoBSi	7560	22.9	120000	35	1.8	12
2605SA1	FeSiB	7190	25.4	45000	27	1.56	30

the GMMs are less readily available in thin foils (important for maintaining a low profile *in situ*) and require much larger biasing fields for optimal operation (on the order of 100 Oe). Preliminary experiments with Terfenol-D samples were unsatisfactory, although further development may prove the material beneficial.

B. Analytical and Numerical Modeling

In our proposed application, the magnetoelastic sensor is affected by the dynamic biological environment. Specifically, the surrounding liquid medium along with sludge accumulation has direct effects on the response of the sensor in terms of both resonant frequency and signal amplitude. To better quantify these effects and to provide insight into the operation of the sensor, an analytical model is proposed. For the following study, the sensor is assumed to be a ribbon (i.e., rectangular in shape), and the length is assumed to be along the x-axis. Also, the sensor is assumed to be fixed only at the exact midlength, resulting in free–free end conditions.

Following a treatment in [15], (1) and (2) can be made 1-D by replacing the magnetostrictivity and stiffness matrices with the isotropic magnetostrictivity and apparent Young's modulus, respectively. Newton's law is then applied to an infinitesimal volume of the sensor loaded on both sides with sludge and vibrating in a viscous medium. The strain in the sludge is assumed to be the same as that in the sensor. The analysis results in the following equation of motion relating the input magnetic field to the sensor displacement:

$$\underbrace{\left[\left(E_{\text{app}} - \frac{E_{\text{app}}^2 d^2}{\mu_0 \mu_r}\right) t_{\text{sens}} + 2E_{\text{sludge}}^* t_{\text{sludge}}\right] \frac{\partial^2 u}{\partial x^2}}_{\text{Stiffness Terms}}$$

$$-\underbrace{\left(\rho_{\text{sens}} t_{\text{sens}} + 1.98\rho_{\text{fl}}\sqrt{\frac{2\nu}{\omega}} + 2\rho_{\text{sludge}} t_{\text{sludge}}\right) \frac{\partial^2 u}{\partial t^2}}_{\text{Mass Loading Terms}}$$

$$-\underbrace{\left(2\mu\sqrt{\frac{\omega}{2\nu}} + \alpha\rho_{\text{sens}} t_{\text{sens}}\right) \frac{\partial u}{\partial t}}_{\text{Viscous Damping Terms}}$$

$$+\underbrace{\left[\beta\left(E_{\text{app}} - \frac{E_{\text{app}}^2 d^2}{\mu_0 \mu_r}\right) t_{\text{sens}}\right] \frac{\partial^3 u}{\partial x^2 \partial t}}_{\text{Hysteretic Damping Term}}$$

$$=\underbrace{E_{app} \text{d} t_{\text{sens}} \cdot H \cdot e^{i\omega t}\frac{d\varphi}{dx}}_{\text{Driving Term}}. \tag{3}$$

E_{app} = Apparent Young's Modulus	t_{sens} = Sensor Thickness
ν = Fluid Kinematic Viscosity	t_{sludge} = Sludge Thickness
u = Local Sensor Displacement	d = Magnetostrictivity
ω = Input Signal Radial Frequency	ρ_{sens} = Sensor Density
φ = Shape Function	ρ_{fl} = Fluid Density
E_{sludge}^* = Sludge Complex Modulus	ρ_{sludge} = Sludge Density
α = Sensor Mass Damping Factor	β = Sensor Stiffness Damping Factor
μ_o = Permeability of Free Space	μ_r = Sensor Relative Permeability
μ = Fluid Dynamic Viscosity	H = Input Field Strength

The derivation of specific terms is described in more detail subsequently. The parameters in (3) are defined as in Table II.

The stiffness of the sensor is modified by the coupling between the strain and the magnetic field, as described in (1) and (2). The sludge is assumed to be a viscoelastic material such that it can be described with a complex modulus possessing a storage aspect in-phase with the displacement and a loss aspect out-of-phase with the displacement [25].

The first and third mass loading terms are simply the mass per unit length of the sensor and sludge, respectively. This assumes a uniform layer of sludge on both sides of the sensor. The second term is an effective mass loading provided by the surrounding viscous fluid, as described in [26]. Briefly, the sensor (or sludge) surface and fluid interact, and a certain amount of the fluid—with a characteristic length dependent on the activation frequency and fluid viscosity—is activated and contributes to the kinetic energy of the vibration.

The first viscous damping term reflects the damping mechanism provided by the surrounding medium due to viscous shear stresses, an effect also described in [26]. The second viscous damping term represents damping that is proportional to the mass of the sensor. The hysteretic damping term represents damping that is proportional to the stiffness of the sensor. The choice of modeling the overall structural damping of the sensor with terms proportional to the mass and stiffness of the sensor is due to the direct comparison that can be made to the damping assigned in the customized finite-element analysis (FEA) model (described later in this section).

The coupling described by (1) and (2) gives rise to the driving term. For this analysis, the interrogative magnetic field H is assumed to be sinusoidal in time and uniform in space. However, because the sensor has a large relative permeability, the actual field within the sensor is not uniform along the length of the sensor. The distribution of the field within the sensor is described by the shape function φ. The shape function is
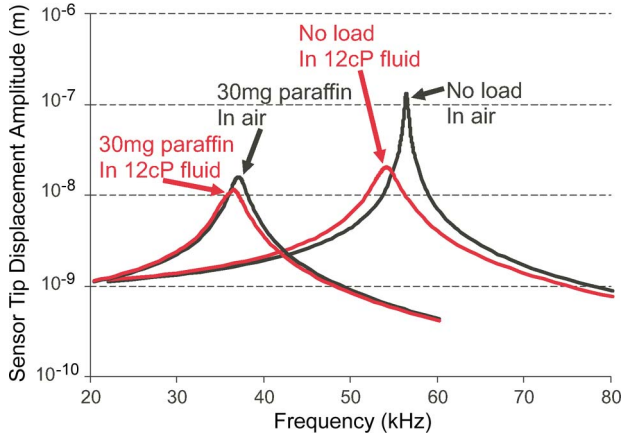
Fig. 4. Model simulation of a 2×37.5-mm-long magnetoelastic sensor displacement frequency response for various loading conditions.

dependent on permeability and, to a lesser extent, on sensor aspect ratio and is determined for the purposes of this analysis by fitting a curve to results determined from a magnetostatic FEA with the desired sensor geometry.

The equation of motion and associated boundary conditions can be solved via the method of eigenfunction expansion, as described in [25]. The result is an infinite summation of eigenfunctions multiplied by a term related to the mass loading terms, damping terms, stiffness terms, and applied magnetic field. Because we are generally concerned with only the first resonant frequency of the system, a one-term approximation is appropriate and justified according to a truncation analysis.

The one-term approximation is as follows:

$$
u(x,t) = \\
-\frac{E_{app} dt_{\text{sens}} H \frac{2}{L} \left[\int_0^L \frac{d\varphi}{dx} \sin\left(\frac{\pi x}{2L}\right) dx \right] e^{i\omega t}}{\left(\frac{\pi}{2L}\right)^2 (k_{\text{eff}}) - \omega^2(m_{\text{eff}}) + i\omega \left[c_{\text{visc,eff}} + \left(\frac{\pi}{2L}\right)^2 c_{\text{hyst,eff}} \right]} \\
\times \sin\left(\frac{\pi x}{2L}\right) \quad (4)
$$

where

$$
k_{\text{eff}} = \left(E_{\text{app}} - \frac{E_{\text{app}}^2 d^2}{\mu_o \mu_r} \right) t_{\text{sens}} + 2E_{\text{sludge}}^* t_{\text{sludge}} \quad (5)
$$

$$
m_{\text{eff}} = \rho_{\text{sens}} t_{\text{sens}} + 1.98 \rho_{\text{fl}} \sqrt{\frac{2\nu}{\omega}} + 2\rho_{\text{sludge}} t_{\text{sludge}} \quad (6)
$$

$$
c_{\text{visc,eff}} = 2\mu \sqrt{\frac{\omega}{2\nu}} + \alpha \rho_{\text{sens}} t_{\text{sens}} \quad (7)
$$

$$
c_{\text{hyst,eff}} = \beta \left(E_{\text{app}} - \frac{E_{\text{app}}^2 d^2}{\mu_o \mu_r} \right) t_{\text{sens}} \quad (8)
$$

and L is the half-length of the sensor, while x is measured from the midlength of the sensor. Results for various loads on a 2×37.5-mm 2826MB ribbon sensor are shown in Fig. 4. Note that the simulation uses values for paraffin as a load [27], rather than values for sludge. This is to facilitate comparison with experimental results in this paper, as described in Section VI. Note that biofilms like sludge are likely to be less stiff than the

test materials used in this paper [28]. According to the model, mass loads that are less stiff tend to have a smaller effect on the amplitude of displacement, which is proportional to the induced voltage on the receive coil in the wireless setup [16]. Thus, the sludge simulants used in this paper are likely to have worst case effects on signal amplitude and full-scale range.

It should be noted here that due to the coupling between stress, strain, field strength, and flux, the sensor will exhibit not only a mechanical resonant frequency, as can be determined from (4), but also an electromagnetic antiresonant frequency when measured with a pickup coil. This phenomenon is given analytical treatment in [16].

The aforementioned analysis provides insight into the operation of ribbon sensors, which have a simple longitudinal vibration mode shape. Because the wishbone-array sensor pattern that is used in the second-generation system presented in this paper represents a significant departure from typical ribbon sensors, we developed an FEA tool that is appropriate for estimating mode shapes and expected signal amplitudes from sensors with complicated structures. The primary component of this tool is the use of (1) and (2) to establish coupling between the magnetic and structural physics domains. For this work, the FEA code is implemented in COMSOL Multiphysics. A detailed look at an FEA implementation for magnetostrictive materials is in [29]; the approach used in this work is modified for specific application to resonant sensors by utilizing time-harmonic (frequency-response) structural and magnetic analysis modes.

The desired sensor geometry is modeled in the FEA program, along with the geometry of the transmit coil. For the purposes of this paper, the FE code was first verified using data from the coaxial test setup (explained in Section V) and a 2×37.5-mm 2826MB ribbon sensor. The current in the transmit coil was measured and applied in the model to generate the field at the sensor. The flux from the sensor response was integrated numerically over the volume of the receive coil to establish the induced voltage. The frequency of the current was swept over an appropriate range, and in this manner, the voltage frequency response of the system could be calculated and compared to experimentally obtained data. Values available in the literature for apparent modulus, permeability, and magnetostrictivity of the material were used, along with reasonable values for proportional damping. Small modifications to the literature values for the material parameters resulted in excellent fit with experimental data, as shown in Fig. 5. These modified values were then used to analyze the complex wishbone-array structure that is used in the second-generation system presented in this paper, with excellent agreement in predicted resonant frequency (within 2% of experimentally measured values for all mode shapes). Trends in the experimentally measured amplitude are also predicted by the FEA (Fig. 5). Also note that displacements calculated with the analytical model for the ribbon sensor match those predicted by the FEA within 10%; the discrepancy between the two is mainly due to a coupled shape function φ that is slightly larger than the shape function calculated with a magnetostatic analysis and used in the analytical model.

In Fig. 6, calculated mode shapes for planar wishbone-array sensors are shown. The mode shapes displayed are at
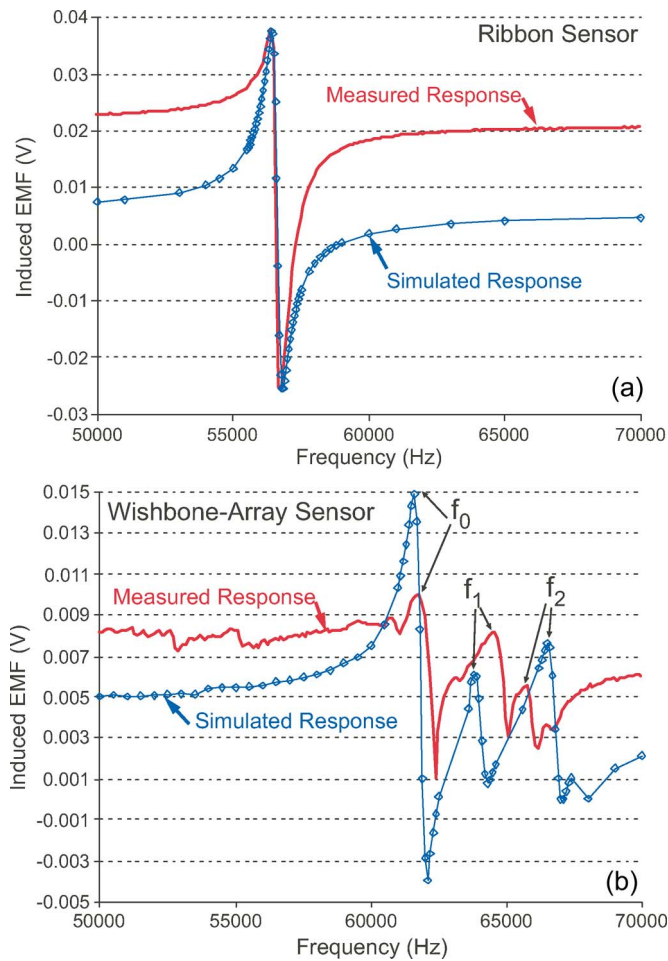
Fig. 5. (a) FEA-calculated and FEA-measured electromotive force (EMF) for a 2×37.5-mm 2826MB ribbon sensor. The measured data were used to optimize parameters in the model (stiffness, damping, and magnetomechanical coupling coefficient). (b) FEA-calculated and FEA-measured EMF for a planar wishbone-array sensor, utilizing the optimal parameters from (a). Note that both resonant and antiresonant behaviors are captured, and predicted frequencies match the measured frequencies within 1.25%. General trends in signal amplitude are also predicted. The discrepancy between the simulated and measured baseline values (far from resonance) may be due to coupling between the transmit and receive coils that is not captured in the finite-element model or due to frequency dependence of the sensor permeability.

frequencies corresponding to peaks in the calculated frequency response for the planar wishbone-array sensors, with the mode shape at 61.6 kHz resulting in the largest response amplitude. Note that the mode shapes combine significant longitudinal and transverse motions, whereas mode shapes of traditional ribbon sensors are limited to longitudinal motion. It will be seen that the transverse motion in these mode shapes leads to a higher sensitivity response of the wishbone-array sensors to viscosity changes.

A final tool used for the design of the wishbone-array sensors was structural FEA to determine the amount of deformation that the sensors could experience without resulting in plastic strain. This is pertinent in our application because biliary stents generally reach their final *in situ* diameter via an elastic self-expansion after a catheter-based delivery. Thus, any sensor integrated with the biliary stent will need to withstand compression onto the delivery system and any subsequent expansion without performance degradation.
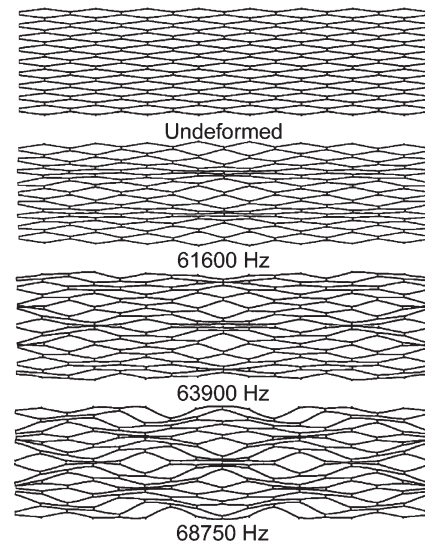
Fig. 6. FEA-calculated mode shapes for a planar wishbone-array magneto-elastic sensor, occurring at the listed frequencies. Note the difference between these shapes and the purely extensional mode of ribbon sensors.

III. DESIGN

A. Generation-1 System

The first-generation system includes a ribbon sensor, a stent, and discrete neodymium magnets that bias the sensor; refer back to Fig. 2(b) for a conceptual sketch of the system. Most commercial self-expanding biliary stents (e.g., those offered by Boston Scientific) rely on elastic expansion of a braided metal mesh. Producing the mesh by braiding filaments limits the inclusion of features that allow the attachment of sensors for enhanced functionality. An investigation into alternative stent designs and fabrication approaches is thus warranted.

Previous work in our group has investigated the advantages of a planar approach to fabrication of cardiovascular stents [30]. In this biliary stent system, a planar approach to fabrication facilitates the inclusion of mechanical features for sensor attachment and stent seam closure. The sensor attachment points in this work take the form of hooks [Fig. 7(b)]. Prior to attaching the sensor, the hooks are folded up so that they stand out of plane. In this manner, the hooks act not only as an attachment point but also as a standoff that provides an operating gap between the sensor and the stent sidewall. The basic pattern of the stent is a diamond mesh, similar to the mesh formed after braiding filaments in the commercial design. The side length of each diamond is nominally 1 mm.

As noted in Section II-A, the resonant frequency of the sensor can be altered by a change in the biasing magnetic field as a consequence of the ΔE effect. In our application, it is envisioned that all interrogative equipment remains external to the patient. Because the orientation of the interrogation equipment with respect to the sensor can vary on a test-to-test or patient-to-patient basis, a dc biasing field emanating from this equipment adds an uncertainty that is reduced by integrating the magnet. Preliminary tests showed that the resonant frequency can shift by 2% with a change in dc bias field orientation of $\sim 45°$.

The permanent magnets must be integrated in such a way as not only to provide a magnetic field of sufficient uniformity
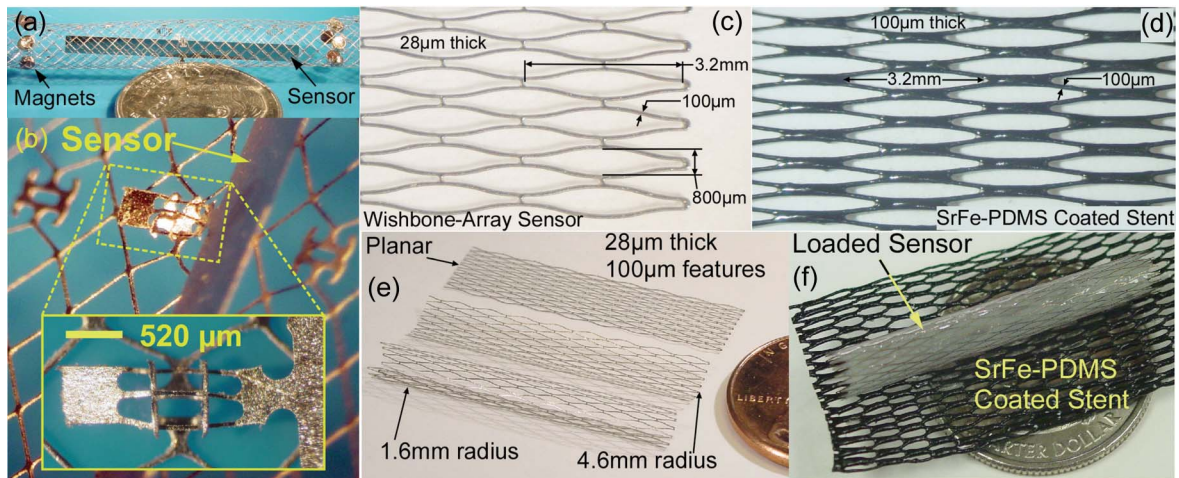
Fig. 7. (a) 2 × 25-mm µEDM'd ribbon sensor. (b) Ribbon sensor attachment to the stent with interlocking features. (c) Microfabricated wishbone-array pattern. (d) Microfabricated self-expanding stent pattern, coated with polymer-suspended SrFe. Notice the similarity in the sensor and stent pattern; this allows for similar flexibility and expansion capabilities in the stent and sensor. (e) Wishbone-array sensors with varying degrees of curvature achieved by thermally annealing the sensor while placed in tubes of various radii. (f) Wishbone-array sensor integrated with SrFe-coated stent and coated with acrylate terpolymer ($\sim$2.3× the sensor mass). The stent seam is not bonded here for visual clarity.

and magnitude to properly bias the sensor, but also to minimally interfere with the expansion of the stent and allow an open lumen to be maintained. For the 37.5-mm-long × 2-mm-wide sensors used in this paper, a bias field strength of 2.5–3.5 Oe is necessary for optimal signal amplitude. A finite-element simulation was performed (Ansoft Maxwell 11.1) using two circumferential rings of six 0.8-mm-thick × 1.6-mm-diameter neodymium magnets (K&J Magnetics). Simulation results show that this configuration can achieve sufficient field strength and uniformity for the needs of this design.

The majority of the reports on the use of rare-earth permanent magnets in biomedical implants are focused on intraoral magnets for dentistry and orthodontic purposes. Although the intraoral environment is not identical to that of the bile duct, these investigations do allow some conclusions to be drawn regarding the biocompatibility of rare-earth permanent magnets. Literature notes that although bare neodymium magnets are susceptible to corrosion in saliva—particularly in the presence of bacteria—a parylene coating is effective in protecting against corrosion [31]. Additional research shows that the response of buccal mucosa (the lining of the cheeks and lips) exposed to a magnetized implant with 80–140-Oe field strength is negligibly different from the response of the same tissue exposed to a demagnetized implant [32]. These findings suggest that a passivated rare-earth magnet of the size and strength that we require does not pose a significant biocompatibility risk.

The basic sensor shape is a ribbon of constant cross section, 2.5 mm wide and 37.5 mm long. The attachment feature on the sensor is an integrated clip at the ribbon midlength. In this work, the clip consists of three beams coupled at the ends [Fig. 7(b)]. This clip is aligned over the hooks on the stent and then brought into engagement with the hooks. As the engagement length increases, the outer beams are deflected over the hooks and eventually snap elastically back into place under the hooks. The middle beam remains on top of the hook and keeps the other beams engaged with the hooks.

B. Generation-2 System

The discrete approach to the magnet and sensor components in the first-generation system is but one design option. Another approach is to use distributed components. Components that conform to or mimic the open flexible structure of the stent would lead to a system that is better able to withstand and accommodate the deformations required during catheter-based delivery, as well as lead to a system that preserves the structural functionality of the stent. With this viewpoint, the second-generation system utilizes a stent coated with a biasing permanent-magnet layer. The sensor used in the second-generation system also conforms to the meshed topology and tubular curvature of the biliary stent.

To improve the elasticity of the stent, chrome–nickel Elgiloy is used. This material has a much higher yield strain than stainless steel ($\sim$1% for Elgiloy versus $\sim$0.15% for 316L stainless steel [33]). Elgiloy is commonly used in self-expanding biliary stents due to the high yield strain and low corrodibility. As shown in Fig. 7(d), an elongated wishbone-array pattern is used; this pattern allows good mechanical flexibility for the stent in a one-piece planar design that can be batch fabricated. This pattern is also used in the sensor, as will be explained later.

Sensor performance is generally improved when the bias field is as uniform as possible. This uniformity is difficult to achieve with integrated discrete magnets because the field strength will necessarily decay as the distance from the magnets increases. However, if the magnetized portion of the system were to be continuously distributed, the field strength could be maintained more uniformly. This improves the sensor performance and eradicates high magnetic field gradients that lead to undesirable magnetic forces.

The distributed magnet is chosen in this paper to be a layer of strontium ferrite (SrFe) particles ($\sim$1-µm average diameter, Hoosier Magnetics, Inc.) suspended in PDMS (Sylgard 184, Dow Corning). This choice is made again in keeping with minimally altering the functionality and structure of the biliary stent with the additional components. In this case,

the polymer-suspended particles can be applied in a thin flexible layer conforming exactly to the stent structure [Fig. 7(d)].

Other polymers have been used as a base for SrFe particles in microfabricated magnets described elsewhere [34]. SrFe particles have the advantages over other magnetizable candidate materials of being chemically inert (owing to their ceramic nature) and of being widely and inexpensively available in very small particle sizes. The chemical inertness is particularly valuable in our implantable application. PDMS is chosen as a base material in this paper due to its generally accepted biocompatibility and due to processing ease. In fact, the entire polymer-suspended magnet fabrication process (as will be described later) is preferable in terms of ease compared with alternative options such as sputtering or electrodeposition of a thin-film magnetic layer. It is well known that PDMS tends to absorb moisture [35]. However, this is not expected to significantly affect the magnetic performance of the layer due to a number of reasons. First, the inertness of the SrFe particles minimizes the potential for the absorbed moisture to alter the magnetic properties of the material. Second, the mechanical deformation of PDMS due to solvent absorption is small (on the order of 2% in common acids and bases [36]), so accompanying geometrical changes in the magnetic field are expected to be insignificant in this application. Finally, the SrFe–PDMS layer can be coated with parylene to further enhance biocompatibility and reduce moisture penetration.

In keeping with the philosophy of mimicking the design of the stent with the design of the magnetoelastic sensor, we would like to use a sensor material with superior elastic properties and to shape the material in diamond-shaped patterns. Fortunately, Metglas alloys are materials with excellent magnetostrictive properties as well as excellent elastic properties. For instance, the 2826MB alloy, as used in this paper, is reported to have a yield strain of 1.6% [37]. This value is even higher than the ~1% yield strains of cold-reduced Elgiloy [38]. Metglas is not, however, readily available in filament form. It is also likely that a resonant sensor fashioned from braided filaments would have low structural coupling and high damping at braid crossover points, limiting efficiency as a resonator. Again, an elongated wishbone-array pattern is used which enhances flexibility while maintaining mechanical coupling and minimizing joint damping for efficient resonant operation of the sensor [Fig. 7(c)].

To ensure that plastic strain in the sensor is avoided during deformation that is required during catheter-based delivery, an FEA model is utilized, with results shown in Fig. 8. With the fabricated dimensions, FEA suggests that the wishbone-array sensor can undergo a 50% reduction in circumference without plastic strain that may result in degradation of sensor performance.

IV. FABRICATION

A. Generation-1 System

For this work, stents are batch fabricated from planar 316L stainless steel foil patterned by photochemical machining (PCM). PCM, or chemical blanking, is a process that utilizes a laser-defined mask to lithographically pattern a photoresist (PR)
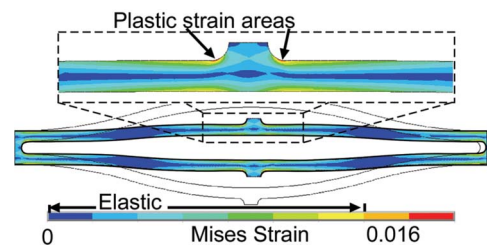
Fig. 8. FEA-calculated strain in a single wishbone cell during cell deformation. The deformation shown corresponds to that required for a reduction in diameter of 50% for the curved array. Only a small area of the wishbone structure exceeds the yield strain with this deformation.
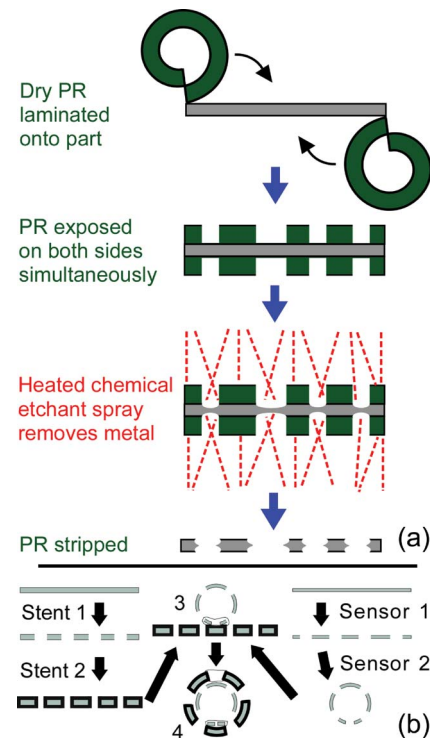
Fig. 9. (a) PCM process flow. (b) Second-generation system fabrication process. (1) PCM patterning of Elgiloy (stent) and Metglas (sensor). (2) Stent coated in SrFe–PDMS layer and magnetized. Sensor annealed in a tube. (3) Sensor anchors bonded to the stent with PDMS. (4) Stent seam bonded with PDMS.

layer covering the base metal layer [39]. The PR is developed, and the unprotected metal is etched with a heated spray of etchant. In this way, intricately patterned flat metal parts can be produced, with thicknesses ranging from 10 μm to 1.6 mm [Fig. 9(a)]. The base metal sheet is typically 300 × 450 mm, although larger sheets can easily be processed.

PCM is derived from printed circuit board etching processes, so the most common PRs and etchants are geared toward processing copper. However, with appropriate surface treatment (to promote PR adhesion) and modified etchants, many other metals can be processed. The PR is typically laminated onto both sides of the base metal layer, and both sides are exposed simultaneously. Typical etchants include ferric chloride, cupric chloride, sodium hydroxide, hydrochloric acid, or even hydrofluoric acid for particularly chemically resistant metals. Among others, copper, aluminum, stainless steel, nickel alloys, platinum, tungsten, and even titanium can be processed with

an appropriate etchant. The etching is an isotropic process, so masks are adjusted for undercut based on the thickness of the part. Feature sizes are constrained by the workpiece thickness, and the minimum feature size is approximately equal to the thickness. For a 50-μm-thick foil, as used in this paper, lateral feature sizes are as small as 33 μm, with external radii as small as 22 μm. Tolerances of $\pm 10\%$ of the part thickness are typical. Material removal rates are approximately 10–50 μm/min, although looser tolerances can allow for faster etching.

The main advantages of PCM include the ability of burr-free processing of thin metal without distortion or other physical changes to the workpiece. Additionally, very hard and brittle metals are machined without difficulty. Of importance to this work, magnetically soft materials can be processed with PCM while retaining optimal permeability—indicating that PCM is an option for processing the magnetoelastic sensor material. Chief disadvantages of PCM include the limitations imposed by the chemistry of the workpiece, as well as the fact that sharp radii cannot be produced due to the undercut involved in the isotropic process.

The thickness of the magnets can be controlled—as may be necessitated by the required bias field—by utilizing a lapping procedure with a diamond slurry. The permanent magnets can be attached to appropriate portions of the stent using a biocompatible adhesive or epoxy. For this preliminary work, a quick-setting epoxy was used to affix the magnets. The magnetoelastic sensors are patterned from 28-μm-thick planar Ni/Fe alloy foil (Metglas 2826MB) by μEDM.

System Assembly: The sensor is attached and the permanent magnets are affixed while the stent is in a planar state. In order to prop open the bile duct as intended, the planar stent must be shaped into a tube. The PCM process allows for deformable mechanical features to be placed on the lateral edges of the planar stent. When the stent is rolled into a tubular shape, these mechanical features can be interlocked such that the tubular shape is maintained. The mechanical features remain inside the tubular profile of the stent, so they do no damage to the duct wall. The stent in its final assembly state is shown in Fig. 7(a).

B. Generation-2 System

The stent is batch fabricated using the PCM process, in this case from a 100-μm-thick foil of Elgiloy. As intended, the feature sizes and patterns are identical to those of the sensor [Fig. 7(c) and (d)]. The overall stent size is 5 mm (diameter) $\times$ 40 mm.

To form the conformal magnetic layer, the PDMS is first mixed in a 10 : 1 base-to-curing-agent ratio. Subsequently, the SrFe particles are introduced in 1 : 1, 3 : 1, or 1 : 3 SrFe-to-PDMS by weight ratios and mixed in by hand until the mixture is consistent (usually about 1 min of mixing time). The mixture is then poured or spread into a mold containing the stent. The stent is then peeled out of the mold, with a conformal layer of the magnetic suspension adhered. The layer is then cured for 30 min at 60 °C. Thicker layers can be built up by repeating the process, although thermally treating the sensor reduces the field—and thus the thickness—required (as shown

in Section VI-A). Finally, the layer is magnetized uniformly along the long axis of the stent using a benchtop pulse magnetizer. In general, the 1 : 1 SrFe:PDMS ratio offered the best combination of workability and remnant strength of the ratios tested.

The wishbone-array sensors for this work are batch fabricated from a 28-μm-thick foil of 2826MB Metglas utilizing the PCM process. Feature sizes of the individual struts are 100 μm. The overall size of the active portion of the sensor (not including the anchor areas to be discussed later) is 7.5 $\times$ 29 mm.

PCM is a planar process, so the as-fabricated sensors are also planar. Because the stent application calls for a generally tubular shape, and the lateral dimension of the sensor is larger than the diameter of the stent, the sensor must be curved into a tubular or semitubular shape to best match the stent geometry. Initial attempts to add curvature to the sensor via elastic bending (e.g., by rolling the sensor and stent into a tube) resulted in a resonant frequency shift and a severe decrease in the amplitude of the sensor signal. This effect is thought to be the result of a combination of mechanical stress imposed in the material as well as geometrical changes in the mode shapes. Instead, the tubular shape is achieved in this work by placing the sensor against the inner wall of a fixture tube and annealing at a high temperature for 30 min [Fig. 7(e)]. By annealing the sensor in the curved state, mechanical stress in the material is relieved while the desired shape is maintained. Note that this thermal treatment is applied to the sensor only, separate from the coated stent. Various final radii can be achieved by either changing the radius of the fixture tube or changing the anneal temperature. For instance, a 4.6-mm radius results from annealing at 375 °C for 30 min inside a 3.6-mm-radius tube, while a 1.6-mm radius results from annealing inside a 1.25-mm-radius tube. Lower temperatures lead to lesser final curvature. The manner in which these treatments affect the sensor performance is detailed in Section VI-A.

System Assembly: Lateral portions of the wishbone-array sensor are connected to the active area with single struts. These portions act as anchors, and the thin flexible struts isolate the vibrating active area from the anchors. The anchors are bonded to the stent with a thin layer of PDMS. Mechanical changes in the PDMS (due to solvent absorption) are not expected to affect the resonant frequency of the sensor because the vibration of the active sensor area is decoupled from the PDMS by the struts. Subsequently, the stent is rolled into a tubular shape, and the resulting seam where the edges of the stent adjoin is also bonded with a thin layer of PDMS. The assembly process is shown in Fig. 9(b), and an assembly is shown in Fig. 7(f).

V. Experimental Methods

Two different wireless coil configurations are used to evaluate the performance of the systems, as shown in Fig. 10. In each case, the transmit and receive coils are driven and measured by an HP 4395A Network Analyzer. The output signal from the 4395A is amplified prior to reaching the transmit coils. The extracorporeal configuration is intended for use in the final application, after the system is implanted. In this setup, coils are configured such that the transmit and receive coils can both
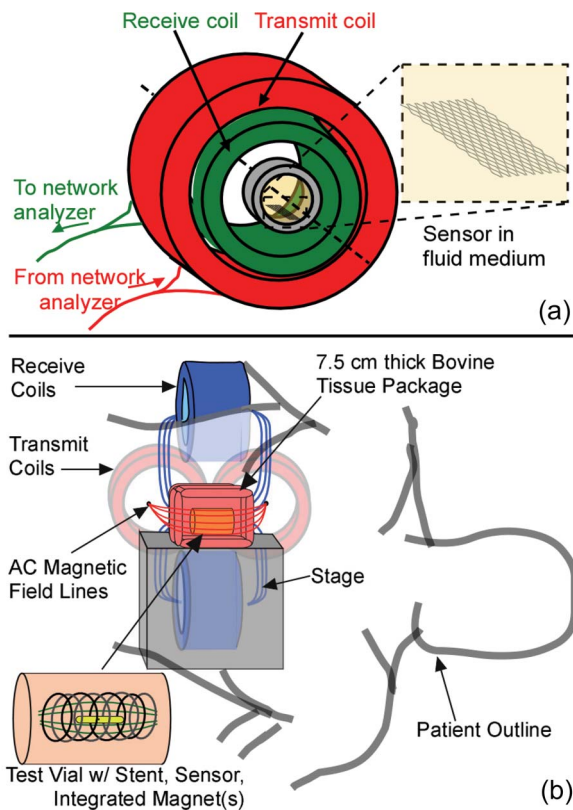
Fig. 10. (a) Coaxial coil configuration. Dual Helmholtz coils (not shown) on either end of the transmit and receive coils can be used to provide a uniform and well-controlled bias field to isolated sensors. (b) Extracorporeal coil configuration. In both configurations, a vial filled with viscous media simulates bile, and in the extracorporeal setup, a 7.5-cm-thick package of bovine tissue can be used to simulate the potential signal attenuation due to the intervening tissue of the patient. Differences between the test setups in the measured signal amplitude were consistent regardless of sensor geometry, sensor material, or sensor environment.

couple to the sensor, but not with each other. The interrogative field lines emanate from one transmit coil, loop through the sensor position such that the field lines are longitudinally aligned with the sensor, and terminate in the other transmit coil. The response field lines emanate from the sensor and are in essentially the same pattern as they would be if emanating from a dipole magnet. Thus, the receive coils are located at a null point of the transmitted signal, are oriented perpendicular to the direction of the transmit field, and yet are aligned with the resulting field from the sensor. This arrangement helps to decouple the transmit signal from the received signal, improving the signal-to-noise ratio. The systems are tested in this setup, both with and without a 7.5-cm-thick package of bovine tissue surrounding the system. The bovine tissue is intended to mimic the intervening tissue of a patient in which the system has been implanted and to help assess any signal degradation due to such tissue.

The coaxial configuration is used for benchtop testing and mainly for initial evaluation purposes. In this setup, transmit and receive coils are concentrically oriented. The device under test is also placed in the center of this setup. With this setup, isolated sensors can be evaluated using a uniform but variable bias field applied by Helmholtz coils located coaxially with the

long axis of the sensor, outside the transmit and receive coils. The main advantages of this setup over the extracorporeal setup are that it easily achieves a higher signal-to-noise ratio and that recorded signal amplitudes are less dependent on precise sensor positioning. However, this setup cannot be used to replicate conditions when the sensor is fully implanted, as concentric coils of the size used would lie inside the patient—which is an obviously undesirable situation. The bile duct runs approximately vertically in an upright patient, so a coaxial wireless setup could be used if the transmit and receive coils were large enough to fully encircle the patient (see [9] for a potential configuration). Important parameters for both the extracorporeal and coaxial test setups are listed in Table III.

When evaluating the field strength of the magnets or magnetic layer, two methods are used. First, a Hall probe (Analog Devices, Inc. AD22151) gives an estimate of the field strength, although the probe does average over a relatively large (0.5×0.5-mm) area. For the first-generation system, this method is sufficient to get a clear picture of the field in the sensor area, as the sensor is located in a uniform portion of the field resulting from the discrete magnets. For the second-generation system, in which the sensor is located very near the magnetic layer, the spatial averaging due to the size of the Hall probe is more of an issue. To address this, the second method of evaluating the field strength is to use a small (1-cm $\times$ 2-mm) ribbon sensor, the performance of which has been characterized for various uniform biasing fields. The small sensor can be placed in different locations along the length of the stent and near the magnetic layer, and the resulting frequency and amplitude of the sensor can be correlated, using the characterized performance in a uniform field, with the local field provided by the magnetic layer. In this way, the ΔE effect of the material is used to evaluate the strength and uniformity of the fabricated magnetic layer.

Bile viscosity changes are precursors to sludge accumulation [40], and bile viscosity varies with sludge content from 1 to 14 cP [41], so sensor response to viscosity is evaluated. The first-generation system is tested by placing the system in a glass vial (2.5-cm inner diameter) filled with water with varying sucrose content [42]. The glass vial is then placed in the appropriate test setup. The viscosity response of the second system and of isolated sensors is tested by using fluids of known viscosities (Dow Corning) in a polycarbonate test vial (1.25-cm inner diameter).

As described in Section II-B, accumulation of sludge results in a mass loading effect on the sensor. For benchtop testing purposes, this process is simulated by the application of one of two different materials—paraffin and an acrylate terpolymer—to as-cast and thermally treated wishbone-array sensors, as well as to as-cast 2.5×37.5-mm ribbon sensors. The paraffin is applied by repeated dip coating. The acrylate terpolymer—commercially available dissolved in a solvent—is either sprayed onto the sensor or brushed on. The two sludge simulants allow a reasonable variation in mass distribution, which is important because sludge accumulation *in situ* is not likely to be perfectly uniform. Additionally, the simulants possess different mechanical properties, so variation in sensor performance due to these differences can be quantified.

TABLE III
COIL CONFIGURATION COMPARISON

	Coaxial[1]	Extracorporeal[2]
Transmit Coil Diameter (cm)	15.7	13
Transmit Coil Turns/Length (1/m)	588	1275
Transmit Coil Length (cm)	8	8.5
Receive Coil Diameter (cm)	10.3	13
Receive Coil Turns/Length (1/m)	614	514
Receive Coil Length (cm)	4.4	7
Longitudinal AC Magnetic Field Amplitude at Sensor (A/m)	20.5	12
Current Amplitude in Transmit Coil (mA)	38	95
SNR for Unloaded 2 mm x 37.5 mm 2826MB Ribbon Sensor (7.5 cm from extracorporeal setup)	210	25

1 – Transmit and receive coils are mounted coaxially and concentrically, with the receive coil inside the transmit coil. The sensor is placed at the center of the coils for testing.
2 – Coils are configured as shown in Fig. 10B, with each coil mounted so no gap exists between adjacent coils. The face of the transmit coils toward the test area is flush with the curved sides of the receive coils; this face is to be positioned on the back of the patient. The nominal sensor position and orientation for testing is as shown in Fig. 10B: in the plane containing the axes of the transmit coils, centrally positioned between the two transmit coils and 7.5 cm away from the face of the transmit coils.

VI. EXPERIMENTAL RESULTS

A. Isolated Sensors

Prior to integration, sensors were tested without the stent in the coaxial test setup while biased with dual Helmholtz coils, as described in Section V. Initial evaluation of four as-cast planar wishbone-array sensors showed that the frequency and amplitude responses versus bias field were similar across the sensors for all important modes, indicating a repeatable PCM fabrication process.

To evaluate the effects of thermal treatments that are used to give the sensors curvature, the wishbone-array sensors were thermally treated either above (375 °C) or below (325 °C) the material Curie temperature (353 °C) and either remained planar or were given curvature. Posttreatment evaluation showed lower optimal biasing field ($\sim$1.5 Oe versus 5-Oe pretreatment) and improved signal level (up to 13.5 mVp-p versus 9 mVp-p pretreatment). This important result shows that thermal treatment allows the use of thinner SrFe–PDMS layers, which simplifies fabrication and minimizes system size, and minimizes concerns about large chronically implanted magnetic fields.

As-cast and thermally treated wishbone-array sensors were compressed through 1.5-mm-diameter tubes—a circumferential deformation of at least 37%—without signal degradation. The repeatable performance of this test across both as-cast and thermally treated sensors implies that the thermal treatment process does not lead to impaired mechanical properties. The slight discrepancy with the FEA model predictions may be due to an imperfect correlation between the onset of plastic strain and the onset of strains that change the magnetomechanical properties of the material.

As-cast and thermally treated wishbone-array sensors, as well as as-cast 2.5 × 37.5-mm ribbon sensors, were evaluated for response to mass loading with both paraffin and acrylate terpolymer. As shown in Fig. 11, each of the sensor types reacts similarly in terms of resonant frequency to both sludge simulants. The variability in the frequency data is likely due to changes in the distribution of the mass from run to run. Repeated tests with a loaded sensor showed a signal amplitude repeatability of 10%–20%, while the frequency repeatability
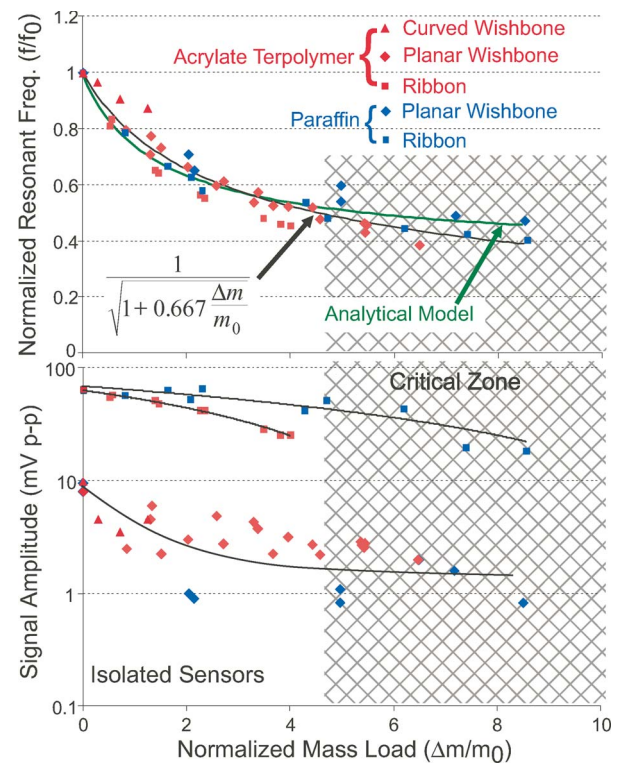
Fig. 11. As-cast planar and thermally treated curved wishbone-array sensors, as well as as-cast ribbon sensors (2826MB, 2 × 37.5 mm), were loaded with either paraffin or acrylate terpolymer layers to simulate sludge accumulation. The curve in the top graph is calculated by minimizing the sum of squared errors between all points and the line using an equation of the form shown. Results for the analytical model (utilizing literature values for paraffin properties) are also superimposed. Lines in the bottom graph are guides to the eye.

was 0.2%–0.5%. Furthermore, the full-scale range of each sensor type extends into the "critical zone." Based on the initial mass of each sensor type, and assuming that the sensors are integrated with 4-mm-diameter stents, the critical zone corresponds to at least 50% occlusion by a uniform layer of sludge. Also, note that the initial amplitude of the ribbon sensors is higher than the initial amplitude of the wishbone-array sensors. However, the amplitude of the ribbon sensors decreases nearly
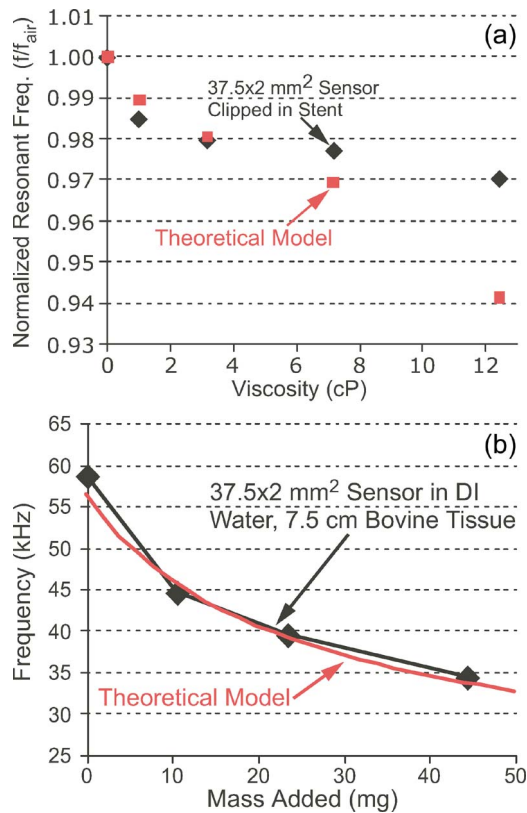
Fig. 12. (a) Frequency versus viscosity for an integrated generation-1 system. (b) Frequency versus mass loading for an integrated generation-1 system. The system is immersed in DI water (1-cP viscosity), and the sensor is loaded with paraffin.

linearly with increased mass loads (with a significant slope that is related to the properties of the loading layer), while the amplitude of the wishbone-array sensors seems to quickly decrease to a plateau and hold that level over nearly the entire tested range. Note that the analytical model predicts that signal amplitude for a ribbon sensor will be decreased most with mass loads from stiffer materials with a high loss modulus; thus, it may be reasoned that the acrylate terpolymer used in this paper is stiffer and has a higher loss modulus than the paraffin.

B. Generation-1 System

As described in Section III-A, the first-generation system includes a ribbon sensor, a stent, and discrete neodymium magnets that bias the sensor. The viscosity response of the system was measured over a physiologically appropriate range using the extracorporeal coil configuration. As shown in Fig. 12(a), the resonant frequency of the magnetoelastic sensors shifted by a total of about 1.7 kHz, or 2.8%, when the viscosity ranged from 0 to 12 cP. This demonstrates sensitivity to viscosity shifts that precede sludge accumulation. This also highlights the importance of having an integrated magnetic field with a constant orientation; as described previously, the ΔE effect can easily result in a 2% frequency shift with a 45° change in field-to-sensor orientation.

Paraffin loading resulted in resonant frequency shifts of 24 kHz, or 40.7%, after a mass of 45 mg has been added, which is in very good agreement with the analytical model proposed

in Section II-B. This mass load represents 2.5× the unloaded mass of the sensor. If the mass is assumed to be distributed in a uniform thickness on the sensor and if the sludge is also uniformly distributed on the stent with the same thickness, then this mass load would represent a significant 29.7% occlusion of a 4-mm-diameter stent due to sludge accumulation. Additionally, it can be seen from Fig. 12(b) that the frequency sensitivity of the sensor has not saturated at this mass load, so the full-scale range of the sensor figures to be even greater than that reached in this test, as illustrated with isolated sensors in part A of this section.

Other important results for this system include the magnetic field delivered by the integrated neodymium magnets, as well as the retention force that is provided by the sensor attachment features. For two rings of six 1.6-mm-diameter × 800-mm-thick neodymium magnets separated by 45 mm, the field measured with the Hall probe was approximately 3 Oe. To test the retention force of the sensor attachment features, three sensors were attached to three different attachment points on three different stents. The stents were held fixed while a tensile load was applied to the sensor at the midlength of the sensor. The tensile load was measured with a load cell (Imada, Inc.), and peak values were recorded. The minimum tensile force withstood for the three samples was 0.367 N, and the attachment is robust enough to withstand simulated catheter deployment.

C. Generation-2 System

As described in Section III-B, the second-generation system consists of a curved wishbone-array sensor and a conformal SrFe–PDMS magnetic layer. To closely compare results for the integrated system to the results obtained for the isolated sensors as described in part A of this section, the coaxial test setup was used. The external dual Helmholtz coils were not used, so the sensor was biased only by the integrated magnetic layer.

The viscosity response of the system was measured over a physiologically appropriate range even as mass was added. As shown in Fig. 13(a), the resonant frequency of the wishbone-array sensors shifted by about 6.5% typically over this range of viscosities and was not significantly affected by mass buildup. Note that the sensitivity over this range is approximately double that of the ribbon sensors. This sensitivity difference is likely due to the different effects that viscous damping has on the transverse motion of the wishbone-array mode shapes. Note that as mass builds on the sensor, the normalized signal amplitude becomes less sensitive to viscosity. This is a trend predicted for the ribbon sensor in the analytical model.

The system was also tested for response to mass loads by successively coating the sensor in acrylate terpolymer. Because of the close integration between the sensor and the stent, it was difficult to apply mass directly to the sensor without also applying some to the stent. As such, the actual load on the sensor was back-calculated from the frequency response curve calculated for the isolated sensors (shown in Fig. 11). Note that the trend seen in Fig. 11 for the wishbone-array sensors in which the amplitude quickly decreases to a plateau is also seen for the integrated system in Fig. 13(b).
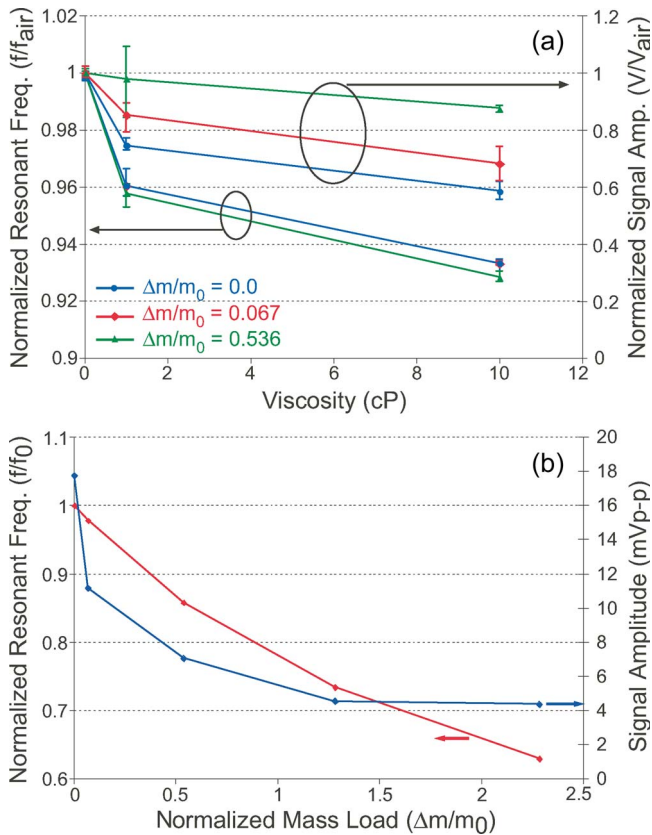
Fig. 13. (a) Response of the generation-2 system to viscosity changes was measured even as mass was added. The resonant frequency of the sensor remains sensitive to physiologically appropriate viscosity changes even with increasing mass loads. Note that as mass is added, the signal amplitude is less sensitive to viscosity changes. (b) Mass was added to the generation-2 system with acrylate terpolymer. The mass that was added directly to the sensor was difficult to separate from the mass that was added to the stent, so the equation shown in Fig. 11 was used to back-calculate the mass load. The signal amplitude of the integrated sensor responds in a manner similar to that of the isolated sensors in Fig. 11.

VII. DISCUSSION

Both of the systems described in this paper exhibited satisfactory performance in critical benchtop tests of frequency response to viscosity and mass loading. The analytical and finite-element models developed for estimating the frequency and amplitude of the response of the sensors, although linearized, proved to be predictive and offer useful insight into the operation of the resonant sensors. Wherever possible, batch fabrication techniques were used. In fact, the techniques used for fabrication of all components in the second-generation system are batch compatible.

Although this paper focused on the integration of sensors with self-expanding metal stents, it is important to note that these sensors can also be integrated with commonly used plastic biliary stents. These plastic stents are essentially polyethylene or polytetrafluoroethylene tubes, typically of 2.5–4-mm-inner diameter and 8–10-cm length. To accommodate the smaller inner diameter of a plastic stent, the sensor width should be reduced, which lowers the signal amplitude of the sensor. For instance, a 1-mm-wide $\times$ 37.5-mm-long ribbon sensor integrated with a plastic stent exhibits signal amplitudes of approximately half those of the 2 $\times$ 37.5-mm ribbon sensor for the same

normalized mass load. These reduced signal amplitudes are still sufficient for detection at a 7.5-cm wireless range. Normalized resonant frequency sensitivity to paraffin loads for the 1-mm-wide sensor is indistinguishable from that of the 2-mm-wide sensor.

Three advantages of the wishbone-array sensor over typical ribbon sensors in this application are evident from the results. First, the fine feature sizes and large open area of the pattern facilitate bile flow, supporting the primary function of the biliary stent. Second, these sensors are much more accommodating of the large deformations required for catheter-based delivery. Third, these sensors have a higher sensitivity to viscosity changes, which is a clinically relevant parameter in many pathological conditions. A limitation of the wishbone-array sensor, at least with the present design, is the smaller signal amplitude. However, since the readout involves a frequency shift, this does not have a direct impact on the utility of the instrument. Preliminary results show that the signal amplitude tends to scale with the overall sensor length, so this disadvantage may be mitigated with a longer sensor design, within the constraints of the length of a typical biliary stent (≥ 40 mm).

Although this paper has shown that wireless magnetoelastic sensing holds fundamental promise for monitoring critical parameters in biliary stents, some secondary issues associated with the application have yet to be formally addressed. One secondary issue is that the amorphous metal has a tendency to corrode. It is not yet clear whether the corrosion products are cytotoxic; however, accelerated testing has shown that the signal amplitude of 6 $\times$ 12.5-mm ribbon sensors decreased by 90.7%, while the resonant frequency decreased by 14%—accompanied by visual evidence of extensive corrosion—after a simulated 12-month immersion in saline. In comparison, sensors coated with 8 μm of parylene and subjected to the same testing showed an average resonant frequency increase of 0.2% and an average signal amplitude increase of 8%—both similar to the repeatability of the sensors. The act of coating the sensor with parylene reduced the signal amplitude by 35%, but thinner coatings may provide sufficient passivation with a smaller effect on the signal amplitude. Another secondary issue is that local curvature of the bile duct may result in contact between the sensor and stent, which may degrade the signal. For instance, imparting a longitudinal radius of curvature of 75 mm to a 37.5-mm-long ribbon sensor via contact resulted in an amplitude decrease of 30%–40%. Future testing should also include quantifying the flexibility and self-expandability of the system, both on the delivery device and after deployment. *In vivo* testing will confirm the useful signal range in an implanted situation, and the response of the sensor to biologically accurate conditions will be exposed.

VIII. CONCLUSION

Systems that integrate biliary stents with magnetoelastic sensors and permanent magnets are investigated for wireless monitoring of direct indicators of restenosis, including shifts in bile viscosity and accumulation of biliary sludge. Two generations of the system are focused on in this paper. The first-generation system integrates a 37.5 $\times$ 2-mm ribbon sensor and neodymium

magnets with a batch-fabricated biliary stent. Paraffin mass loads up to 45 mg simulated sludge accumulation, resulting in a 40.7% resonant frequency shift. As viscosity is varied from that of healthy bile to that of diseased bile, a resonant frequency shift of 2.8% was measured.

The second-generation system integrates a flexible wishbone-array magnetoelastic sensor and a conformal magnetic layer with a batch-fabricated biliary stent. The system is sensitive to physiologically appropriate viscosity changes, showing a 6.5% decrease in resonant frequency in 10-cP fluid. The system is also capable of measuring mass buildup that is associated with sludge accumulation, showing a 38% decrease in the resonant frequency after an applied mass load of $2.3\times$ the mass of the sensor. The integrated system is robust to deformations required for delivery, provides a uniform biasing layer that minimally affects stent mechanics, and represents a much improved form factor over the first-generation system. Appropriate scaling of this sensing methodology could allow use in stents of all kinds, including coronary and ureteral stents.

REFERENCES

[1] G. Donnelli, E. Guaglianone, R. Di Rosa, F. Fiocca, and A. Basoli, "Plastic biliary stent occlusion: Factors involved and possible preventive approaches," *Clin. Med. Res.*, vol. 5, no. 1, pp. 53–60, Mar. 2007.

[2] K. Takahata, Y. Gianchandani, and K. Wise, "Micromachined antenna stents and cuffs for monitoring intraluminal pressure and flow," *J. Microelectromech. Syst.*, vol. 15, no. 5, pp. 1289–1298, Oct. 2006.

[3] P. Howard, G. Murphy, and R. Dowling, "Gall bladder emptying patterns in response to a normal meal in healthy subjects and patients with gall stones: Ultrasound study," *Gut*, vol. 32, no. 11, pp. 1406–1411, Nov. 1991.

[4] E. vanSonnenberg, J. Ferrucci, C. Neff, P. Mueller, J. Simeone, and J. Wittenberg, "Biliary pressure: Manometric and perfusion studies at percutaneous transhepatic cholangiography and percutaneous biliary drainage," *Radiology*, vol. 148, no. 1, pp. 41–50, Jul. 1983.

[5] C. Grimes and P. Stoyanov, "A remotely interrogatable magnetochemical sensor for environmental monitoring," in *Proc. IEEE Aerosp. Conf.*, 1998, pp. 87–92.

[6] P. Stoyanov and C. Grimes, "A remote query magnetostrictive viscosity sensor," *Sens. Actuators A, Phys.*, vol. 80, no. 1, pp. 8–14, Mar. 2000.

[7] C. Grimes, D. Kouzoudis, and C. Mungle, "Simultaneous measurement of liquid density and viscosity using remote query magnetoelastic sensors," *Rev. Sci. Instrum.*, vol. 71, no. 10, pp. 3822–3824, Oct. 2000.

[8] M. Jain, Q. Cai, and C. Grimes, "A wireless micro-sensor for simultaneous measurement of pH, temperature, and pressure," *Smart Mater. Struct.*, vol. 10, no. 2, pp. 347–353, Apr. 2001.

[9] K. Ong, X. Yang, K. Zeng, and C. Grimes, "Magnetoelastic sensors for biomedical monitoring," *Sens. Lett.*, vol. 3, no. 2, pp. 108–116, Jun. 2005.

[10] C. Grimes, C. Mungle, K. Zeng, M. Jain, W. Dreschel, M. Paulose, and K. Ong, "Wireless magnetoelastic resonance sensors: A critical review," *Sensors*, vol. 2, no. 7, pp. 294–313, Jul. 2002.

[11] K. Zeng and C. Grimes, "Wireless magnetoelastic physical, chemical, and biological sensors," *IEEE Trans. Magn.*, vol. 43, no. 6, pp. 2358–2363, Jun. 2007.

[12] S. Green, M. Richardson, F. Shariff, and Y. B. Gianchandani, "Photochemically patterned biliary stents with integrated permanent magnets and deformable assembly features for wireless magnetoelastic tissue growth sensing," in *Proc. IEEE Int. Conf. Solid-State Sens., Actuators, Microsyst. Transducers*, Jun. 2007, pp. 213–217.

[13] M. Richardson, S. Green, and Y. B. Gianchandani, "Magnetoelastic wireless sensing of tissue growth for self-expanding biliary stents," in *Proc. IEEE Int. Conf. MEMS*, 2007, pp. 469–472.

[14] S. Green and Y. B. Gianchandani, "Wireless biliary stent system with wishbone-array resonant magnetoelastic (WARM) sensor and conformal magnetic layer," in *Proc. IEEE Int. Conf. Solid-State Sens., Actuators, Microsyst.*, Hilton Head, SC, 2008, pp. 158–161.

[15] *Handbook of Giant Magnetostrictive Materials*, G. Engdahl, Ed. New York: Academic, 2000.

[16] T. O'Dell, "Measurement of magnetomechanical coupling factor in amorphous ribbons," *Phys. Stat. Sol. (A)*, vol. 74, no. 2, pp. 565–572, 1982.

[17] Metglas, Inc. [Online]. Available: http://www.metglas.com

[18] A. Clark and M. Wun-Fogle, "A new method of magnetostrictivity and magnetostriction measurement," *IEEE Trans. Magn.*, vol. 25, no. 5, pp. 3611–3613, Sep. 1989.

[19] M. Hyoung Kim, K. Shik Lee, and S. Ho Lim, "Magnetostriction measurements of metallic glass ribbon by fiber-optic Mach–Zehnder interferometry," *J. Magn. Magn. Mater.*, vol. 191, no. 1, pp. 107–112, Jan. 1999.

[20] J. Zhai, S. Dong, Z. Xing, J. Li, and D. Viehland, "Giant magnetoelectric effect in Metglas/polyvinylidene-fluoride laminates," *Appl. Phys. Lett.*, vol. 89, no. 8, p. 083 507, Aug. 2006.

[21] J. D. Livingston, "Magnetomechanical properties of amorphous metals," *Phys. Stat. Sol. (A)*, vol. 70, no. 2, pp. 591–596, 1982.

[22] P. Anderson, III, "Magnetomechanical coupling, ΔE effect, and permeability in FeSiB and FeNiMoB alloys," *J. Appl. Phys.*, vol. 53, no. 11, pp. 8101–8103, Nov. 1982.

[23] C. Modzelewski, H. Savage, L. Kabacoff, and A. Clark, "Magnetomechanical coupling and permeability in transversely annealed Metglas 2605 alloys," *IEEE Trans. Magn.*, vol. MAG-17, no. 6, pp. 2837–2839, Nov. 1981.

[24] X. Zhao and D. Lord, "Application of the Villari effect to electric power harvesting," *J. Appl. Phys.*, vol. 99, no. 8, p. 08M 703, Apr. 2006.

[25] J. C. Snowdon, *Vibration and Shock in Damped Mechanical Systems*. New York: Wiley, 1968.

[26] C. Darvennes and S. Pardue, "Boundary effect of a viscous fluid on a longitudinally vibrating bar: Theory and application," *J. Acoust. Soc. Amer.*, vol. 110, no. 1, pp. 216–224, Jul. 2001.

[27] S. Severtson and M. Nowak, "Dynamic mechanical properties and low-velocity wetting behavior of plastic crystalline states for n-alkane blends," *Langmuir*, vol. 17, no. 16, pp. 4990–4996, 2001.

[28] A. Cense, E. Peeters, B. Gottenbos, F. Baaijens, A. Nuijs, and M. van Dongen, "Mechanical properties and failure of streptococcus mutans biofilms, studied using a microindentation device," *J. Microbiol. Methods*, vol. 67, no. 3, pp. 463–472, Dec. 2006.

[29] J. Benatar, "FEM implementations of magnetostrictive-based applications," M.S. thesis, Univ. Maryland, Baltimore, MD, 2005.

[30] K. Takahata and Y. B. Gianchandani, "A planar approach for manufacturing cardiac stents: Design, fabrication, and mechanical evaluation," *J. Microelectromech. Syst.*, vol. 13, no. 6, pp. 933–939, Dec. 2004.

[31] M. Wilson, H. Kpendema, J. Noar, N. Hunt, and N. Mordan, "Corrosion of intra-oral magnets in the presence and absence of biofilms of *Streptococcus sanguis*," *Biomaterials*, vol. 16, no. 9, pp. 721–725, Jun. 1995.

[32] L. Bondemark, J. Kurol, and A. Larsson, "Long-term effects of orthodontic magnets on human buccal mucosa—A clinical, histological and immunohistochemical study," *Eur. J. Orthod.*, vol. 20, no. 3, pp. 211–218, Jun. 1998.

[33] *Metals Handbook*, ASM Int., Bilthoven, The Netherlands, 1990. ASM International Handbook Committee.

[34] L. Lagorce and M. Allen, "Magnetic and mechanical properties of micromachined strontium ferrite/polyimide composites," *J. Microelectromech. Syst.*, vol. 6, no. 4, pp. 307–312, Dec. 1997.

[35] W.-J. Chang, D. Akin, M. Sedlak, M. Ladisch, and R. Bashir, "Poly(dimethylsiloxane) (PDMS) and silicon hybrid biochip for bacterial culture," *Biomed. Microdevices*, vol. 5, no. 4, pp. 281–290, Dec. 2003.

[36] J. Lee, C. Park, and G. Whitesides, "Solvent compatibility of poly(dimethylsiloxane)-based microfluidic devices," *Anal. Chem.*, vol. 75, no. 23, pp. 6544–6554, Dec. 2003.

[37] J.-J. Lin and T.-P. Perng, "Embrittlement of amorphous $Fe_{40}Ni_{38}Mo_4B_{18}$ alloy by electrolytic hydrogen," *Metall. Mater. Trans., A Phys. Metall. Mater. Sci.*, vol. 26, no. 1, pp. 197–201, Jan. 1995.

[38] Elgiloy Specialty Metals. [Online]. Available: http://www.elgiloy.com
[39] *ASM Handbook*, vol. 16.   Bilthoven, The Netherlands: ASM Int., 1989.
[40] H. Zhang, T. Tsang, C. Jack, and J. Pollack, "Role of bile mucin in bacterial adherence to biliary stents," *J. Lab. Clin. Med.*, vol. 139, no. 1, pp. 28–34, Jan. 2002.
[41] D. Jungst, A. Niemeyer, I. Muller, B. Zundt, G. Meyer, M. Wilhelmi, and R. del Pozo, "Mucin and phospholipids determine viscosity of gallbladder bile in patients with gallstones," *World J. Gastroenterol.*, vol. 7, no. 2, pp. 203–207, Apr. 2001.
[42] D. Lide, Ed., *CRC Handbook of Chemistry and Physics*, 85th ed. Boca Raton, FL: CRC Press, 2004.

Scott R. Green received the B.S. degree in mechanical engineering from Rose-Hulman Institute of Technology, Terre Haute, IN, in 2003.

He held a position as Senior Design Engineer at Stryker Corporation in the Instruments Division before attending the University of Michigan for graduate studies. He has been named as an inventor on two issued or pending U.S. patents. His research interests include design of medical devices and micromachined sensors and actuators.

Yogesh B. Gianchandani received the B.S., M.S., and Ph.D. degrees in electrical engineering, with a focus on microelectronics and MEMS.

He is currently a Professor with the University of Michigan, Ann Arbor, with a primary appointment in the Department of Electrical Engineering and Computer Science and a courtesy appointment in the Department of Mechanical Engineering. He is temporarily with the National Science Foundation, Arlington, VA, as the Program Director within the Electrical, Communication, and Cyber Systems Division. He was previously with the University of Wisconsin, Madison. He also held industry positions, working in the area of integrated circuit design. His research interests include all aspects of design, fabrication, and packaging of micromachined sensors and actuators and their interface circuits. He is the author of approximately 200 papers in journals and conference proceedings and is the holder of about 30 issued or pending U.S. patents. He was a Chief Coeditor of *Comprehensive Microsystems: Fundamentals, Technology, and Applications* (Elsevier, 2007). He serves on the editorial boards of several journals.

Dr. Gianchandani was a General Cochair of the IEEE/ASME International Conference on Micro Electro Mechanical Systems in 2002.